Utrecht University Repository

Title	Development of a bioreactor and volumetric bioprinting protocol to enable perfused culture of biofabricated human epithelial mammary ducts and endothelial constructs
Authors	Buchholz, Maj-Britt; Bernal, Paulina Nunez; Bessler, Nils; Bonhomme, Camille; Levato, Riccardo; Rios, Anne
Published in	Biofabrication
Publication Date	2025-07-01
Link	https://dspace.library.uu.nl/handle/1874/476976
Citation	Buchholz, M-B, Bernal, P N, Bessler, N, Bonhomme, C, Levato, R & Rios, A 2025, 'Development of a bioreactor and volumetric bioprinting protocol to enable perfused culture of biofabricated human epithelial mammary ducts and endothelial constructs', Biofabrication, vol. 17, no. 3, 031001. https://doi.org/10.1088/1758-5090/add20f
Versions / License	Publisher version
Rights	https://www.uu.nl/en/university-library/license-and-reuse-conditions

International Society for Biofabrication
PURPOSE-LED PUBLISHING™

NOTE

Development of a bioreactor and volumetric bioprinting protocol to enable perfused culture of biofabricated human epithelial mammary ducts and endothelial constructs

To cite this article: Maj-Britt Buchholz *et al* 2025 *Biofabrication* **17** 031001

View the article online for updates and enhancements.

You may also like

- A novel membrane-on-chip guides morphogenesis for the reconstruction of the intestinal crypt-villus axis
Sara Sibilio, Raffaele Mennella, Vincenza De Gregorio et al.
- 3D bioprinting of human iPSC-derived cardiac constructs with microvascular network support for improved graft survival *in vivo*
Léa Pourchet, Laura Casado-Medina, Yvonne Richaud-Patin et al.
- Combinatorial strategy for engineering cartilage and bone microtissues using microfluidic cell-laden microgels
Suntae Kim, Siyuan Li, Seung Yeop Baek et al.

This content was downloaded from IP address 131.211.105.245 on 28/08/2025 at 08:22

IOP Publishing Biofabrication 17 (2025) 031001 https://doi.org/10.1088/1758-5090/add20f

Biofabrication

NOTE

RECEIVED
6 September 2024

REVISED
2 April 2025

ACCEPTED FOR PUBLICATION
29 April 2025

PUBLISHED
13 May 2025

Development of a bioreactor and volumetric bioprinting protocol to enable perfused culture of biofabricated human epithelial mammary ducts and endothelial constructs

Maj-Britt Buchholz[1,2], **Paulina Nunez Bernal**[2], **Nils Bessler**[1,3], **Camille Bonhomme**[4], **Riccardo Levato**[2,4,*] **and Anne Rios**[1,3,*]

[1] Princess Máxima Center for Pediatric Oncology, Heidelberglaan 25, 3584 CS Utrecht, The Netherlands
[2] Department of Orthopaedics, University Medical Center Utrecht, Uppsalalaan 8, 3584 CT Utrecht, The Netherlands
[3] Oncode Institute, Utrecht, The Netherlands
[4] Department of Clinical Sciences, Faculty of Veterinary Medicine, Utrecht University, Yalelaan 108, 3584 CM Utrecht, The Netherlands
[*] Authors to whom any correspondence should be addressed.

E-mail: r.levato@uu.nl and a.c.rios@prinsesmaximacentrum.nl

Keywords: biofabrication, volumetric bioprinting, perfusion bioreactor, organ-on-a-chip

Supplementary material for this article is available online

Abstract

Tissue function depends on the 3D spatial organization of cells, extracellular matrix components, as well as dynamic nutrient gradients and mechanical forces. Advances in biofabrication technologies have enabled the creation of increasingly sophisticated tissue models, but achieving native-like tissue maturation post-fabrication remains a challenge. The development of bioreactors and microfluidic systems capable of introducing dynamic culture platforms and controlled mechanical and biochemical stimulation for biofabricated tissue analogues is therefore imperative to address this. In this technical note, we introduce a multi-step pipeline to fabricate, seed and perfuse geometrically complex hydrogel constructs with quality control protocols through the computational analysis of confocal multispectral 3D imaging data for each step of the process. Employing ultra-fast volumetric bioprinting, chips with tunable channel architectures were fabricated. Furthermore, an autoclavable and transparent perfusion bioreactor inspired by open-source designs was developed to enable controlled, long-term perfusion (up to 28 days) and real-time monitoring of cell behavior. As proof-of-concept, employing this pipeline, we fabricated a human mammary ductal model and an endothelialized vessel on-a-chip, demonstrating the compatibility of the platform with epithelial and endothelial cell lines, and investigated the effect of dynamic culture on tissue-specific cell organization. Dynamic perfusion underlined the influence of mechanical stimulation on cell organization and maturation. Various chip architectures, capable of recapitulating tissue-specific features (*i.e.* lobules) were printed, enabling the mono- and co-culture of human mammary epithelial and endothelial cells. Our pipeline, with the accompanying protocols and analysis scripts presented here, provide the potential to be applied for the dynamic culture of a wide range of tissues.

1. Introduction

It has long been recognized that tissue function relies on the 3D spatial organization of cells, matrix components and growth factors [1, 2] as well as dynamic nutrient and oxygen gradients and mechanical forces applied onto and by cells [3]. While *in vivo* animal models are valuable in biomedical research to study cell behavior in a native environment, their predictive capacity is greatly limited, due to interspecies differences [4]. Existing human *in vitro* models, on the other hand, lack complexity to faithfully recapitulate tissue function [5, 6]. To combat these issues, the field of biofabrication has made great strides on making increasingly more architecturally complex tissue models [7, 8]. However, while biofabrication

© 2025 IOP Publishing Ltd. All rights, including for text and data mining, AI training, and similar technologies, are reserved.

allows the precise control over cell and biomaterial patterning, full tissue maturation, essential for proper biological function, can often not be achieved solely by depositing cells into their desired location and must occur through measures taken post-fabrication [9]. Therefore, many bioreactors [10, 11] and microfluidic systems [12, 13] have been developed to provide flow or other (mechanical) stimuli to different tissue constructs to improve cell viability [14], migration [15], differentiation [16], morphogenesis [17] and nutrient- as well as oxygen transport [14, 18].

In this technical note, we introduce a novel and versatile methodology to converge volumetrically bioprinted [19] chip constructs with microfluidics to enable the fabrication of a geometrically complex and perfusable bioprinted hydrogel constructs. We provide landmarks on how to seed the chips and computationally assess printing accuracy, seeding efficacy and cell alignment, as well as organization. We combine the bioprinted chips with the rapid in-house production of an autoclavable and transparent CNC milled perfusion bioreactor to enable dynamic cell culture. This bioreactor, inspired by available open-source designs [20], allows for perfusion, as well as imaging access from top and bottom, enabling the real-time monitoring of cells within bioprinted chips. It further enables direct tissue access, for additional manipulation or subsequent analysis, a feature often lacking in organ-on-a-chip systems [21, 22].

As a proof of concept, we demonstrate the compatibility of our platform with both epithelial and endothelial cells, ensuring applicability across multiple tissue types. Our proposed biofabrication pipeline is applied to modeling human mammary gland (MG) and endothelial tissues, which rely heavily on their intricate 3D architecture and cellular organization—features that conventional 2D and 3D culture systems cannot faithfully mimic [23, 24]. Here, using the high-speed volumetric bioprinting (VBP) approach, we can recapitulate ductal geometries with a widely used, biocompatible hydrogel (gelatin methacryloyl; gelMA) to direct cellular organization of mammary epithelial cells (MCF10A) and endothelial cells (human umbilical vein endothelial cells; HUVECs). We demonstrate that healthy human mammary epithelial cell lines react to flow with more recapitulative organization and polarization than non-flow controls, mirroring in part the biological impact of milk flowing through the duct system that has a crucial role in the upkeep of secretion and production of milk [25–28]. We further leverage VBP's freedom of design to generate more complex ductal architectures by introducing small, curved protrusions throughout the printed channels, mimicking to some extent the lobular units of the MG. The resulting chip, together with additional surface features produced by the VBP process, can be used to influence cell alignment and invasion into the surrounding hydrogel. By further introducing a second channel to our chip constructs seeded with endothelial cells, we demonstrate the possibility of creating complex, multicellular tissue-like models within a compliant hydrogel and combined with dynamic perfusion. Such a dynamic culture platform could be further exploited to exert spatiotemporal control over bioactive cue presentation, in the case of the present breast model, for instance, to introduce hormonal stimulation, essential for mammary tissue homeostasis. With this novel pipeline, we present an open-source workflow that can enable better mimicry of complex cellular processes that cannot easily be studied with current human *in vitro* models. The methodology and technological solutions, as well as computational methods provided here are aimed at facilitating access and adoption of on-a-chip and bioreactor systems and help researchers address key bottlenecks in consistent cell seeding and perfusion culture within their custom-designed models. In addition, all design specification and computer-aided-design (CAD) files for the bioreactor and cell seeding aid devices are provided in an open science framework (OSF) repository. Herein, by combining the power of VBP with an adapted perfusable bioreactor and relevant computational analysis workflows, we have engineered a vascularized human breast model system that could, in the future, be applied to study human MG biology in health and disease. Through this proof of concept, we open the door for the translation of this platform towards other target tissues that can benefit from dynamic culture or for advanced disease modeling.

2. Results and discussion

2.1. Chip design and production

The field of microphysiological systems has become one of the most advanced in the creation of complex *in vitro* models, as they enable the microscale recapitulation of functional tissues and organs [29, 30]. In particular, devices such as organ-on-a-chip platforms have been developed for a myriad of biomedical applications, from disease modeling, toxicity testing, and the study of multi-tissue interactions [30]. The most rudimentary method for modeling tubular tissues in these devices involves casting the desired biomaterial around a removable needle to create simple, straight channel-on-chip designs (figure 1(a)). While efficient when dealing with stiff materials, developing these molded chips with soft, biocompatible hydrogels presents some limitations. In this study, gelMA was selected as the base chip material because of its wide adoption in the tissue

engineering and biofabrication fields, given its tunability and inherent resemblance to native extracellular matrix components [31]. Further, gelMA has extensively been used as a material to study the culture of mammary epithelial cells and cell lines as well as endothelial cells, including the study of their adhesion and migration [32–35]. When molding chips from gelMA using the needle approach, however, cell seeding attempts showed very low efficiency. The number of cells that remained within the channel long enough to attach was low and highly variable between samples, and large amounts of cells were observed passively floating out of the chip altogether. As a visual demonstration, the same tendency was observed when injecting fluorescent beads within these straight, horizontal channels, which were also highly prone to elicit air bubble formation when plugging the chip closed (figures 1(b) and (c)). Consequently, a U-shaped chip design was developed in which the cells were not able to float out of the chip but rather were forced inside the duct by gravity (figure 1(d)). Channel diameters ranged from 500–1000 μm depending on the experiment, which is well within the range of macro tubular native structures, and, pertaining to our proof-of-concept, is also in the range of normal mammary duct diameters ($\sim$750 μm at $\sim$4 mm distance to the nipple) [36]. Since this curved design could not be easily casted with a needle-pull-out approach, we turned to 3D printing technologies, which more easily enable the fabrication of complex, out-of-plane structures, and have been widely used for the production of organ-on-a-chip devices [37]. In this study, we employed VBP to enable the shaping of gelMA hydrogels into these more complex chip structures, given its high printing speed, design freedom, and compatibility with hydrogels and living cells [19]. Light-doses between 180 and 260 mJ cm^{-2} (printing time = 20–30 s) enabled the fabrication of open channels. A comparison between the original CAD files and the 3D reconstructions of printed chips—obtained through light sheet microscopy—via nominal actual comparison in CloudCompare showed a strong resemblance to the reference model (figures 1(e), (g) and suppl. figure 1(a)). Overall, printed chips were slightly larger than reference models, likely due to swelling of the hydrogel post-printing. The average deviation from the original CAD model was 1.94 $\pm$ 2.96% within acceptable ranges ($\pm$7% nominal vector deviation) with lowest deviations in X and Y direction ($\pm$5%) and highest deviations in Z direction (=longitudinal axis of the printer vial; $\pm$20%), occurring at low frequencies, only in specific locations of the print (figures 1(i)–(k)). For instance, at the edges of the chip and the inlets of the duct, over-polymerization could be observed. We compared the over-polymerized areas to the predicted light-intensity accumulations provided through Apparite software and found that all printing deviations were in line with the predicted 3D model-specific accumulation of light intensities in these regions (figures 1(f) and (h)). The correlation between local light-intensity accumulation and print accuracy is therefore a useful tool that can be employed to locally optimize CAD models to improve overall printing outcomes. Together, these results demonstrate that our technique allows for the production of chips with curved, hollow, and perfusable channels that accurately resemble the original CAD model and facilitate cell retention upon seeding.

2.2. Seeding of volumetrically bioprinted chips

With the possibility to create complex channel structures using VBP, a consistent cell seeding strategy, and a method to assess seeding efficiency were also established. Cell seeding to form a confluent layer along the whole channel surface can be achieved by turning the chip in regular intervals [20]. Therefore, a rotating station was implemented to enable the automated rotation of multiple chips simultaneously. The sample holder was designed to fit chips mounted inside bioreactors as well as chips mounted within multi-well plates (figure 2(a), suppl. figure 2(a)). As a proof-of-concept, MCF10A cells were chosen as a well-characterized epithelial cell line reflecting normal human mammary epithelium. Initial testing of the seeding station using 30 million MCF10A/ml showed that rotation of the chips allowed for an even seeding around the whole channel surface (figure 2(b) left, suppl. video 1), as opposed to non-rotated samples where cells predominantly stuck to the bottom of the channel (figure 2(b) right). Cell and channel segmentation were performed in Imaris software and cell coverage of the seeded channels were calculated from a custom-built python script (figure 2(c), suppl. figure 1(b)), which is provided in our open-source repository [38].

Optimal seeding conditions were tested on 6% w/v gelMA as this provided an optimal stiffness (Young's modulus of 8.4 $\pm$ 2.6 kPa) to keep printed channels open. Seeding was also optimized for HUVECs mixed with mesenchymal stem cells (MSCs), to demonstrate the applicability of the developed platform to endothelial structures, given the open challenge of creating and studying vascularized tissue models *in vitro*. Both MCF10A and HUVECs/MSCs did not attach well on gelMA-only chips (coverage = 49.54 $\pm$ 16.17%). Therefore, poly-L-lysine, L-Dopamine and collagen-1, which have previously been reported to improve endothelial and epithelial cell attachment in microfluidic devices, chip systems and on gel surfaces including gelatin-based hydrogels [39–42] were investigated. Furthermore, different cell seeding densities were tested (7.5–60 million cells ml^{-1}) (figures 2(d)–(i), suppl. figure 2(b)). For MCF10A, coating with poly-L-lysine (PLL) led to significantly better cell attachment (coverage = 88.23 $\pm$ 14.5%) than on non-coated chips

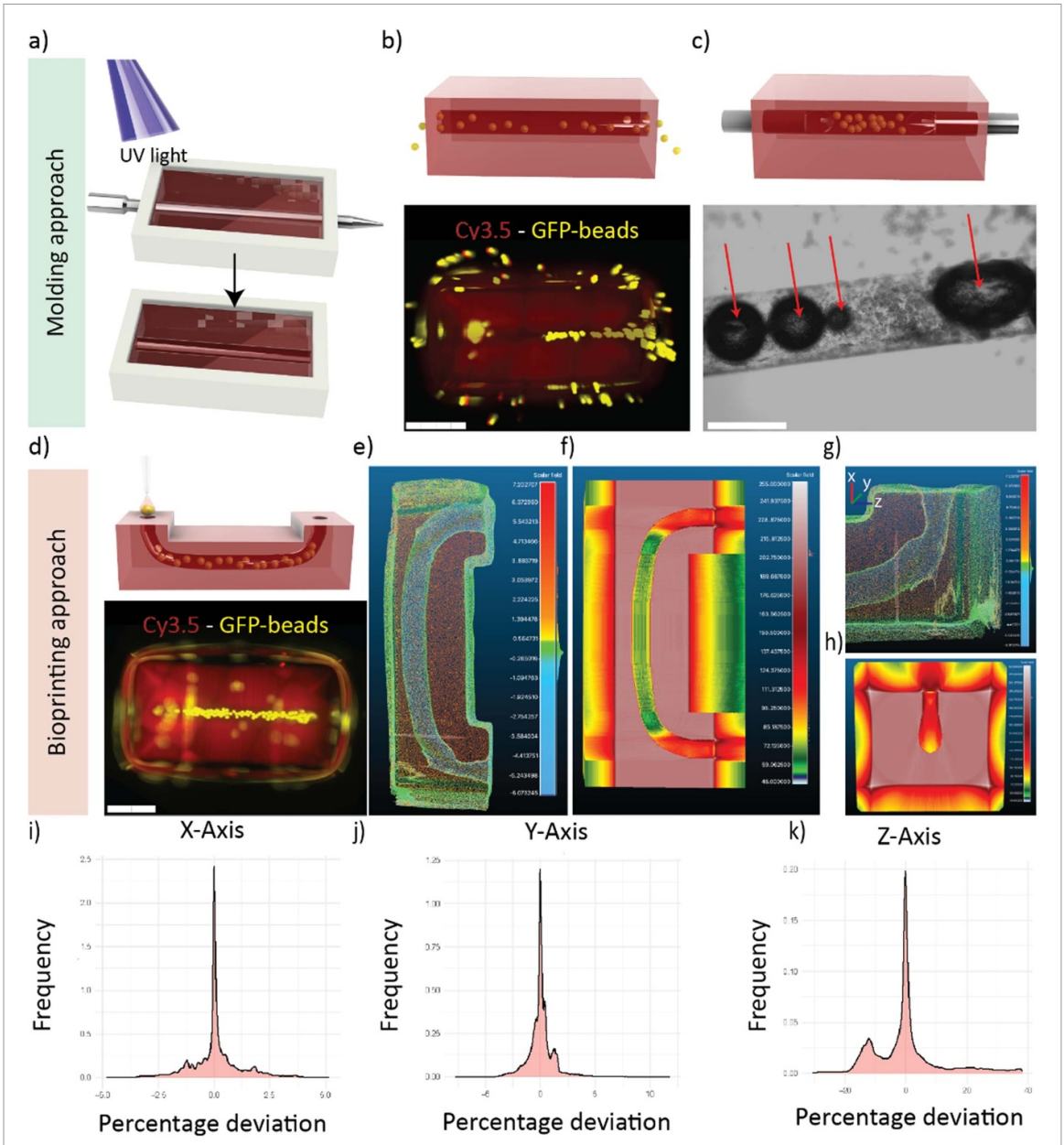

Figure 1. Chip design considerations and printing quality. (a) Schematic of molding approach. (b) Schematic illustration and fluorescent image of issue with cells floating out of the chip, represented by fluorescent beads. Scale bar = 2 mm. (c) Schematic and bright-field (BF) image of air bubbles (red arrows) arising from inserting plug. Scale bar = 1 mm. (d) Schematic and fluorescent image of U-shaped chip designs which allows for more reliable cell seeding here illustrated by the injection of fluorescent beads. Scale bar = 2 mm. (e) Percentage deviations of the printed chip from original CAD model. (f) Predicted light intensity normalized to the median light intensity over the whole 3D model. (g) Percentage deviation of printed chip zoom in showing narrowing of the channel at the inlets. (h) Cross section of predicted light intensity at the channel inlet. (i)–(k) Printing accuracy for *X*, *Y* and *Z* coordinates.

(coverage = 48.59 ± 22.18%) or collagen-1 coated chips (coverage = 49.43 ± 31.7%) (figures 2(d) and (e)). Low (7.5 M cells ml^{-1}) as well as high (60 M cells ml^{-1}) MCF10A seeding densities yielded a high channel coverage (83.82%–88.39%) within a week after seeding (figure 2(g)), suggesting that the initial seeding density does not significantly influence the channel coverage within the chosen range. Notably, when working with lower cell densities (<60 M cells ml^{-1}), sometimes gaps in cell coverage could be observed, which could be closed by employing a second round of cell seeding 3 days after the initial seeding (suppl. figure 2(c), red circles). In order to reduce the necessary amount of cells and to avoid possible cell clumping sometimes seen when using high cell densities (60 M cells ml^{-1}) (suppl. figure 2(c), yellow circles), a density of 30 M MCF10A/ml and double seeding, which is in a similar range as reported for similar breast-on-a-chip models [29], was chosen to obtain uniformly seeded channels. Regarding channel endothelialization through HUVEC/MSC seeding, channel coverage was lower (coverage = 66%–77%) compared to MCF10A (83.82%–88.39%) when seeded on PLL

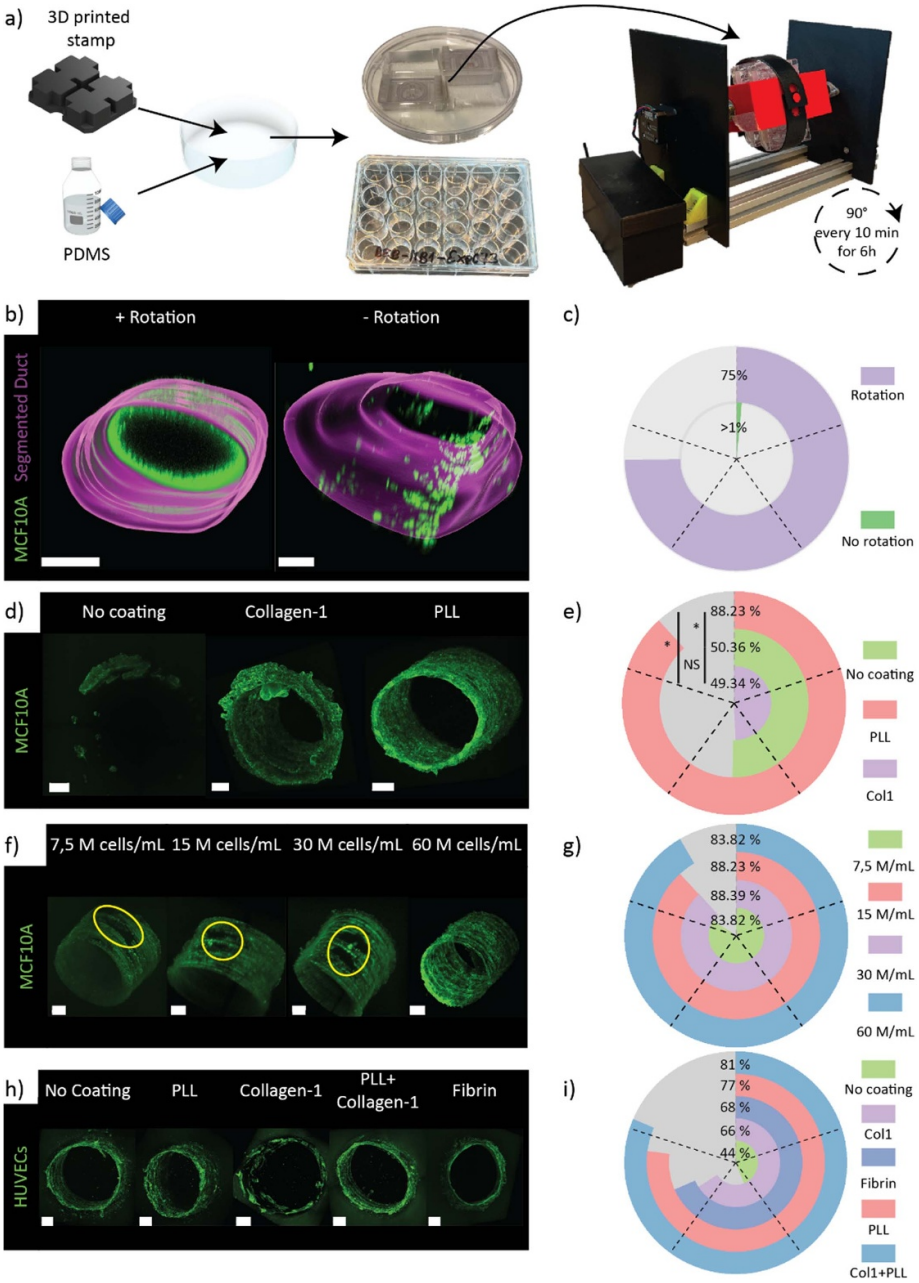

Figure 2. Seeding setup and optimization. (a) Schematic of rotation setup. (b) Fluorescent images of chips seeded with (left) and without (right) rotation. (c) Percentage of the channel surface covered by cells with and without rotation. (d) Channels seeded with MCF10A with different coatings. (e) Percentage of the channels (length = 9 mm diameter = 1 mm) covered with cells with different cell coatings. (f) Channels seeded with different densities of MCF10A and (g) percentage channel coverage. (h) Channels seeded with HUVECs at 20 M cells ml^{-1} with different coatings. (i) Channel coverage of HUVECs with different coatings. Scale bars = 100 μm. Images were taken one week after cell seeding. Differences in cell coverage according to One-way ANOVA were not significant due to sample size unless indicated otherwise (* for $p < 0.05$).

and collagen-1 coated channels. Therefore, we tested the combination of collagen-1 and PLL, as well as a fibrin coating, which has previously been successful in retaining endothelial cell attachment [43]. While fibrin coating did not yield an improved cell coverage, a 1:1 mix of collagen-1 with PLL resulted in 81% cell coverage, although an increased sample size will be necessary to confirm whether this improvement is significant. This coating formulation was subsequently used for all endothelial seeding experiments (figures 2(h) and (i)). Our data demonstrates that different cell types might require different coatings for optimal attachment. As both mammary epithelial cells as well as endothelial cells are in their native environment exposed to a basal lamina [44, 45], future research will be directed at mimicking the basal lamina by the use of laminin-containing coating materials.

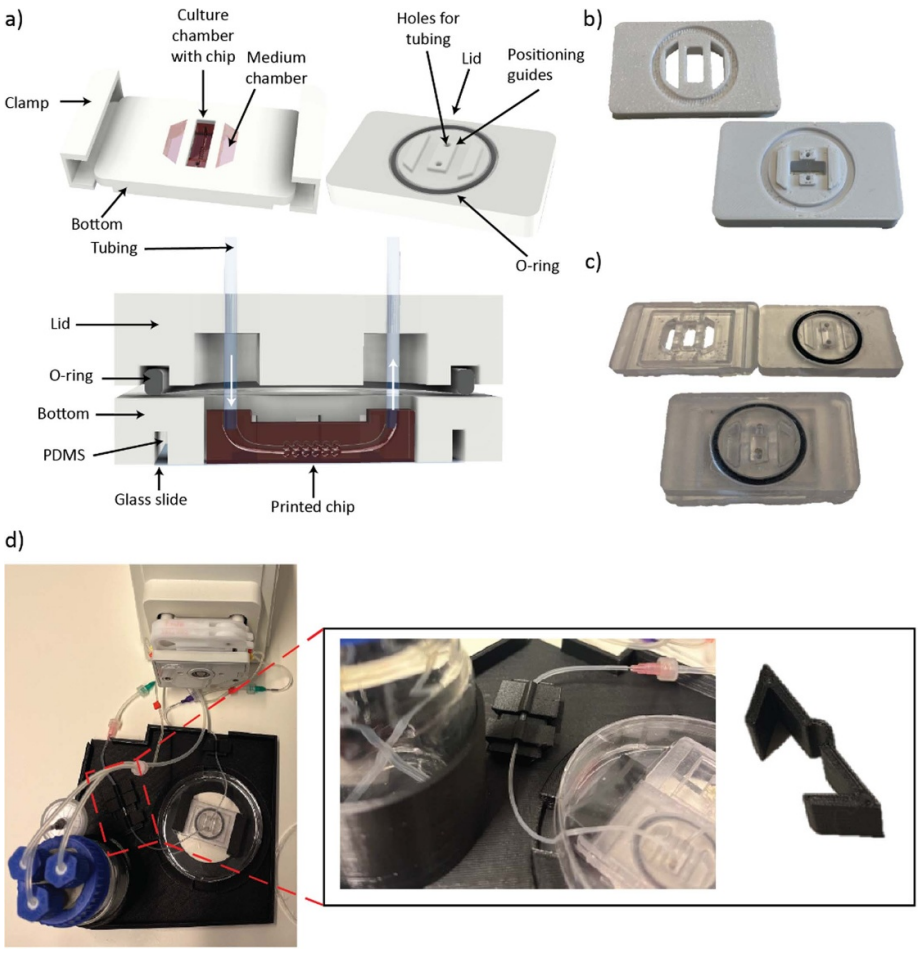

Figure 3. Bioreactor setup. (a) Schematic of bioreactor parts and functions. (b) 3D printed bioreactor. (c) CNC machined bioreactor. (d) Perfusion setup. Zoom in: Tubing clips.

2.3. Development and fabrication of a perfusion bioreactor accessible for imaging

To provide additional functionality to previously reported bioreactors published by Kinstlinger *et al* [20], we developed our own bioreactor design to allow for the perfused culture of ductal cell seeded hydrogel chips. We introduced a thin glass coverslip (0.1 mm thickness) at the bottom of the device to enable cell monitoring using inverted microscopy. Additionally, to prevent the hydrogel-based chips from drying out and enable the use of different media types outside and inside the channel, we included two medium chambers placed at the sides of the central housing for the chip. A lid with two entry ports to plug in fluidic tubing was designed to permit perfusion starting from the top of the hydrogel-based constructs (figure 3(a)). The lid was equipped with guiding extensions, which keep it in place so that the tubing inlets are accurately positioned on top of the channel inlets. The bioreactor is closed with 3D printed clamps applying pressure of the lid onto an O-ring embedded in the bottom part of the bioreactor to prevent leakage. These clamps can easily be slid off to enable access to the cultured tissue for the addition of cells or post-culture analysis.

Bioreactors were initially 3D printed from polyethylene terephthalate glycol (PETG) using fused deposition modeling (FDM) (figure 3(b)). However, the small access window in the lid (formed by a cover slip) did not provide enough visual access to the chip, impeding the installation of tubing for perfusion. Further, if bioreactor were used more than once, chips in 3D printed bioreactors were prone to infections, likely due to the layered microtopography providing an extensive surface area and roughness for bacterial adhesion [46] and the inherent porosity of FDM printed objects, making thorough cleaning difficult as well as wear down over times of use, hampering proper sealing. Therefore, after optimizing the dimension and features for perfusion of the printed chips, final reusable bioreactors were produced from autoclavable transparent polycarbonate via CNC milling, yielding transparent bioreactors, which allowed for infection-free long-term tissue culture (figure 3(c)). All bioreactor parts were autoclaved before each use. No reduction in transparency could be observed over time (5–10 autoclaving cycles). Critical for our bioreactor design was the ability to perfuse from the top due to the advantages of a curved channel design for cell seeding (See section 2.1

Chip design and production). Therefore, tubing inlets had to be incorporated into the bioreactor lid, preventing the use of a glass slide to retain visual access to the chip. The chosen transparent polycarbonate as a bioreactor material allowed us to insert tubing from the top, while maintaining visual access and providing additional sterility, due to the possibility to be autoclaved.

2.4. Perfusion influences mammary epithelial cell organization and barrier function

After seeding, hydrogel-based chips were transferred to the bioreactor after cells had enough time to attach firmly (3 d). When needles were inserted into the chip to initiate perfusion, the chips frequently ruptured at the interface between the soft hydrogel and hard metal (data not shown). Therefore, flexible fishing tubing was used, forming a smoother transition between tubing and gel. This soft tubing was able to adapt to the shape of the chips rather than disrupt it by following the curvature of the duct inlets. The tubing was inserted through the holes of the bioreactor lid and into the chip until the curvature of the channel gave a palpable resistance. Tubing was secured from moving by adding 3D printed tubing clips (figure 3(d)). At the beginning of the culture period, chips were initially perfused at low flow settings (80 μl h^{-1}) for the first two days to prevent not yet fully attached cells from detaching. After initiation of perfusion some cell detachment was observed. However, cell detachment was minor, and cells quickly repopulated the resulting gaps. Under dynamic perfusion (400 μl h^{-1}), cyclic, pulsatile channel expansion and recovery of the bioprinted hydrogel lumen were observed, leading to a decrease/increase of channel width of up to 4% in response to the pulsatile flow (figures 4(a) and (b); Suppl. video 2,3). This demonstrates that chips made from 6% w/v gelMA, as opposed to traditional PDMS chips [47], are highly compliant, similar to native tubular and flow-subjected tissues, a crucial characteristic for the ability to respond to and transmit mechanical forces to cells [30]. The use of a compliant hydrogel is therefore advantageous in the context of microfluidics as it enables the study of tangential, axial, and circumferential shear stresses, which are known to affect endothelial barrier function, cell alignment, morphology, proliferation, migration, and remodeling [48–50]. Flow-induced mechanical forces have also been shown to play a role in epithelial organization, barrier function, and migration [51–55]. Indeed, after one week of perfusion, MCF10A cells started to infiltrate the surrounding gelMA (figure 4(c), right), forming sprouts around the channel of an average length of 195 $\pm$ 68 μm and up to 338 μm in length, as opposed to statically cultured chips, where no sprouting was observed over the culture period (figure 4(c)). After two weeks of dynamic culture (400 μl h^{-1}), cell-free and statically cultured and perfused cell-seeded channels were injected with FITC-inulin and leakage was assessed over time via live imaging to assess epithelial barrier function. As expected, due to the absence of barrier-forming cells, FITC-Inulin leaked out of cell-free channels leading to a 2.9-fold increase of FITC signal outside the channel. Furthermore, FITC-inulin leakage from statically cultured MCF10A chips was observed (1.97 fold increase of FITC signal outside the channel), while perfused channels mostly retained FITC-Inulin inside the channel lumen (1.2 fold increase of FITC signal outside the channel) for the whole duration of imaging (>1 h), demonstrating an increased epithelial barrier function induced by flow (figures 4(d) and (e); supplementary video 4, suppl. figure 1(c)), as has been previously demonstrated for a variety of epithelial cell types [51–55]. Subsequently, chips were stained for breast epithelial markers, CK14 (basal), CK8/18 (luminal), E-cad (breast epithelial) as well as DAPI (nuclei) and Phalloidin (membranes) and imaged using multispectral 3D imaging [56]. Imaging data indicated that the application of flow led cells to properly organize and polarize into a CK14 positive outer cell layer and a CK8/18 positive luminal cell layer, while non-perfused chips displayed a more random organization (figures 4(f) and (g)). Indeed, quantification of cells covering the inner edge of the duct using a custom python script (suppl. figure 1(d)) confirmed that 91.14 $\pm$ 11.57% of the cells were positive for K8/18 in perfused channels, while only 47.04 $\pm$ 2.59% were K8/18 positive on non-perfused channels. Further, a trend was observed where 77.95 $\pm$ 2.73% of the cells covering the inner edge of the perfused duct were not only K8/18 positive but also followed by an outer layer of K14 positive basal cells, displaying correct luminal-basal organization (figures 4(h) and (i)). This demonstrates that the application of flow through our bioreactor design is able to guide cellular organization of epithelial ductal models post-printing through mechanical stimulation and delivers an indication of the important role that flow plays in the organization and polarization of mammary epithelial cells, an important factor influencing functional maturation [57]. While the above mentioned changes in cell barrier function and organization could already be observed after two weeks, we were able to keep samples in perfused culture for up to four weeks without leakage of the system, infections or noticeable deformation of the matrix material. Future research will have to elucidate the exact timing of cellular processes induced by flow stimulation, as well as optimal timing and intensity of flow in these long-term perfusion cultures but is out of the scope of this technical note.

2.5. Guiding cell alignment and invasion through micro-and macro-topographical features

During printing and seeding optimization, we frequently observed striped topographies in printed chips on their *x,y*-plane (figure 4(c)). This has

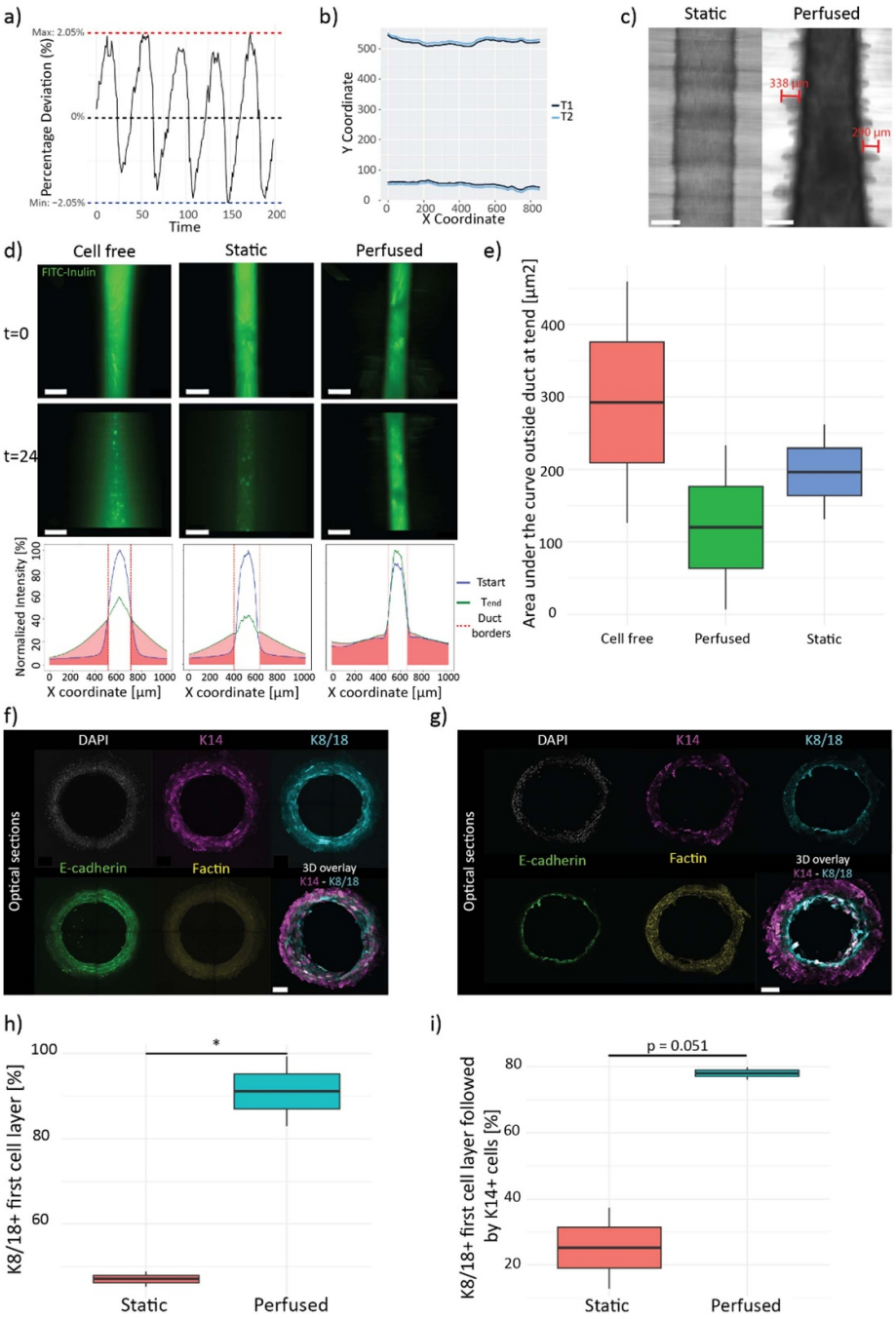

Figure 4. Influence of perfusion on cellular organization of mammary epithelial cells. (a) Percentage expansion patterns of channels under perfusion. (b) Plot of the channel edges at maximum and minimum distance. (c) BF images of perfused and non-perfused channels showing cell invasion into the surrounding tissue for perfused chips as assessed through measurements in Fiji. Scale bar = 500 μm. (d) FITC-Inulin perfusion into seeded channels and FITC quantification outside the channel boundaries over time, as well as (e) quantification of the area under the curve outside of the channel boundaries, demonstrating epithelial barrier function under perfusion. Scale bar = 500 μm. (f) Immunofluorescent images of non- perfused and perfused chips (g). Scale bar = 100 μm. (h) Percentage of cells lining the inner edge of the duct that are K8/18 positive. (i) Percentage of cells lining the duct for which the inner layer is K8/18 positive and is followed by K14 positive cells. Data was acquired after two weeks of perfusion. Differences between culture conditions were not statistically significant due to sample size unless indicated otherwise (* for $p < 0.05$) as calculated through One-way ANOVA (e) and unpaired t-test (h), (i).

previously been explained: if static, laser light projections using a coherent light source are delivered onto a non-rotating vial, straight microfilaments and channels can be formed in the printed object, due to laser speckle patterns [58]. This results in the formation of finely striated prints upon rotation of the resin vat during the VBP process [59]. It should be noted that, if a smooth surface is required, there are protocols in place to remove striations post-printing entirely [59, 60]. However, since cell alignment is known to be influenced by the microscale surface topographies, such as grooves and fibers [3, 61, 62], we investigated how the intrinsic striation elicited by VBP could be leveraged to guide cell alignment

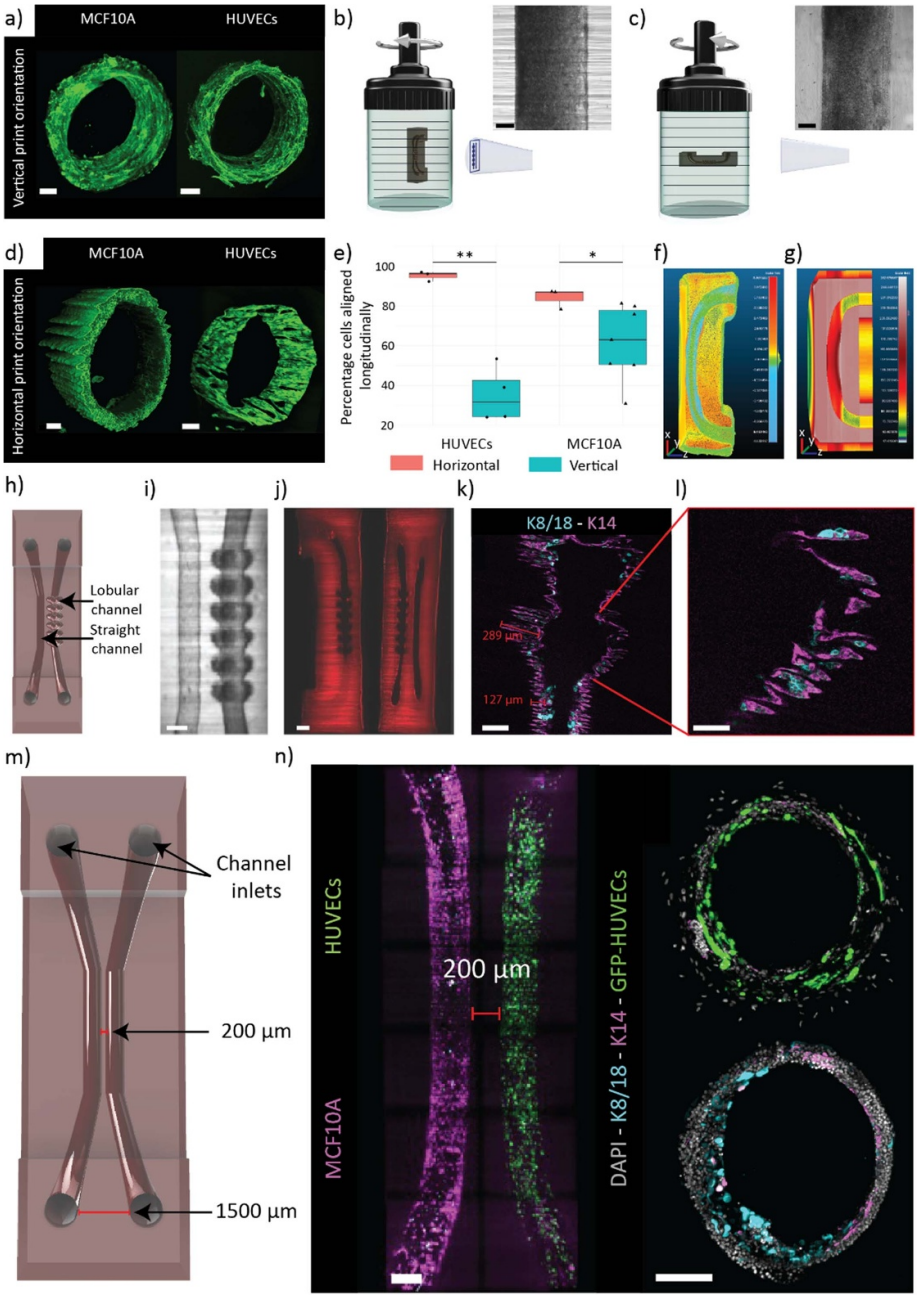

Figure 5. Strategies to improve model maturation. (a) Fluorescent images of chips seeded with MCF10A or HUVECs displaying cellular alignment along the channels circumference. Scale bar = 100 μm (b) Schematic and BF images of chip printed in vertical orientation. Scale bar = 250 μm. (c) Schematic and BF images of chip printed in horizontal orientation. Scale bar = 250 μm. (d) Fluorescent images of horizontally printed chips seeded with MCF10A or HUVECs displaying longitudinal cell alignment. Scale bar = 100 μm. (e) Quantification of cell alignment by print orientation. (f) Nominal comparison of horizontally printed chip indicating reduced channel diameters along longitudinal axis. (g) Computed light intensities over the model when printed horizontally indicating high light accumulation within horizontally printed part of the duct. (h) Schematic, BF images (i) and fluorescent images (j) of chip containing an epithelial duct with lobular structures. Scale bar = 1 mm. (k) Fluorescent image showing MCF10A invasion from the lobular structures (k). Scale bar = 200 μm (k) scale bar = 100 μm (l) (m) schematic of chip with two channels of 200 μm distance. Scale bar = 200 μm. (n) Fluorescent images of 2-channel chip demonstrating the separate culture of these two cell types. Scale bar = 200 μm. Statistical significance of differences between vertically and horizontally printed chips was assessed using Welch's t-test (** for $p < 0.01$; * for $p < 0.05$).

in our printed channels. We observed that, when printing the chip construct vertically (as shown in figure 5) both endothelial and epithelial cells aligned concentrically along the printed channel following concentric striations created during the printing process (figure 5(a)). Notably, cell alignment could be steered by changing print orientation, and by printing the chips in a horizontal orientation striations were aligned along the longitudinal axis of the channel (figures 5(b) and (c)). Upon seeding, segmentation of the cells covering the channel surface revealed that this change in the directionality of striations significantly influenced cellular alignment for both MCF10A and HUVECs, which, when seeded on horizontally

printed chips, aligned along the longitudinal axis of the channel (figures 5(d) and (e); suppl. figure 1(e)) displaying a more native-like orientation [63]. However, it should be noted that this change of print orientation made it more difficult to correctly resolve and print open channels. Nominal actual comparison between CAD model and printed chips showed that over polymerization in horizontally printed chips could occur along the channel, reducing the channel lumen dimensions (figure 5(f)) in line with the increased expected light accumulation in this area (figure 5(g)). Given the limited contrast between in- and off-target voxels, this resulted in prints that are highly susceptible to small variations in the bioresin reactivity, for instance, due to batch-to-batch variation in the hydrogel formulation. Knowing of the increased likelihood of over polymerization within the channel, only chips with 1 mm duct diameter in the CAD design were printed horizontally, accommodating for the expected reduction in channel diameters and leading to a higher success rate in printing chips in a horizontal orientation. While these microtopographies instructed cellular alignment, previous results of Nelson *et al*, on mammary epithelial cells have demonstrated the guidance of epithelial cell migration behavior through instructive geometries. Mammary epithelial cells preferably branched into the surrounding tissue at local maxima of convexity [24]. To investigate whether this observation could be applied to our printed constructs, we therefore introduced small lobular units along the duct, to provide maximum convexity for the MCF10A cells in our platform (figures 5(h)–(j)). Indeed, together with the striations and the fluid movement introduced by the peristaltic pump, the newly introduced lobules lead to MCF10A invasion into the surrounding tissue. This invasion reached depths of 189 $\pm$ 57 μm and was higher in those convex lobular regions than in ductal regions (79.9 $\pm$ 20.2 μm) (figures 5(k), (l) and supplementary figure 3(a)). Furthermore, cell invasion was led by K14 positive basal cells followed by K8/18 positive luminal cells (figures 5(k)–(l)), confirming that the introduction of macro-topographical features such as convexity provides sufficient instruction for the cells to invade their surroundings and possibly initiate branching morphogenesis. Conclusively, our data demonstrates that VBP can be used to introduce micro- and macroscale geometrical cues which guide cellular organization and tissue invasion.

2.6. Increasing model complexity: development of a multicellular chip platform

Having set up a workflow to generate perfused epithelialized or endothelialized ductal models, we explored different strategies to increase cellular heterogeneity, to potentially enhance tissue maturation and biomimicry of the desired tissues in future studies.

A key element of organ-on-a-chip systems, is the ability to recreate multicellular or multi-tissue interactions [29]. To demonstrate this potential application of our chip platform we first showed the possibility to print more than one channel and seed different cell-types in each one, in this case demonstrating the creation of a vascularized mammary duct model as a proof-of-concept. To facilitate targeted cell seeding in this two-channel system, we adjusted the design to include an x-shaped curvature (figure 5(m)), since printing channels in close proximity (200 μm) initially made it challenging to inject cells into their designated channel. By increasing the distance between the inlets while maintaining a small channel separation, we improved the precision of cell seeding with multiple cell types (MCF10A and HUVECs/MSCs). Chips were cultured in 1:1:1 MSC:HUVEC:MCF10A media under static conditions. Channels were injected with their respective culture medium, and epithelial and endothelial cells remained in their respective separate compartments. The smallest vascular-to-epithelial channel distance achieved was 200 μm (figure 5(n)), and at this distance, no branching or sprouting towards the other cellular compartments was observed. Future studies should focus on the optimization of the inter-channel spacing to ensure the desired cellular interactions can take place within the developed chip platform. Alternatively, the introduction of stromal cells directly into the printed chip could be employed to enhance intercellular interactions between seeded channels, and to better simulate native tissue composition and organization. Since VBP is a mild, contactless process, it allows the incorporation of cells and larger cellular units such as organoids sensitive to stresses from other printing methods [19, 64, 65]. Here, we demonstrated the feasibility of printing the developed chip platform in the presence of MSCs (supp. figure 4(a)). These cells represent a stromal component that can be tailored to fit tissue-specific requirements. Cells remained viable (>90% viability) for a 2-week period (supp. figure 4(b)), and the mechanical properties of the printed chip remained constant during this time (supp. figure 4(c)), suggesting that cell incorporation into the bioresin would not significantly affect the stability of the chip.

The developed perfusable platform introduced in this study has the potential to enable the study of complex biological processes in a reproducible, quality controlled fashion. Having established the possibility to produce more native-like chip platforms, further modifications to the system could be introduced to target tissue-specific requirements such as the introduction of materials that better mimic the ECM composition of the tissue of interest—such as granular [66], ECM-derived [67] or dynamic [68], light-sensitive hydrogels compatible with the VBP process—or the introduction of channel/cell-specific growth factors and/or hormones to induce a

more physiological environment for cells to mature as well as the use of more heterogeneous and representative cell sources such as organoids.

3. Conclusions

In this technical note, we presented a biofabrication pipeline including VBP of ductal chips, cell seeding, perfusion bioreactor/platform development and instructions for perfused culture. We further provide five different imaging-driven analysis pipelines addressing printing accuracy, cell coverage, cell alignment and construct maturation. We provide open access to all CAD models needed for the fabrication of the chip, bioreactor, rotator and perfusion platform, as well as all analysis scripts in our OSF repository [38]. Our pipeline is set up to be easily adapted for changes in the experimental setup (i.e. addition of a second channel or more complex geometrical cues) and, therefore, has the potential to be translated to various ductal types of tissue such as kidney, gut, or the presently demonstrated mammary duct and vascular applications. With these pipelines and analysis scripts we aim to contribute to aiding the development of more advanced organ-on-a-chip models with clearly defined and accessible readout parameters.

We applied our pipeline for the production of biomimetic chips using established epithelial and endothelial cell lines and show that VBP delivers chips of high print accuracy. We demonstrate the influence of micro- and macro-topographical features on cell alignment and invasion into the surrounding tissue and show that flow-induced shear stress and repetitive stretching of our compliant hydrogel chips improve mammary luminal-basal epithelial cell organization and barrier function.

Since the aim of this technical note was to provide a framework for the production and seeding of chip structures that can be applied to various tissue types, we restricted our biomaterial choice to gelMA and different materials for channel coating. Tissue-specific changes in matrix composition could, therefore, be the subject of further investigation and it has to be noted that cell behavior, amongst others attachment, might differ across materials of different stiffnesses. Future research aimed at improving model maturation could include steps, such as the incorporation of additional stromal cell types, hormonal stimulation or changes in culture conditions, including hypoxia [69]. As a proof-of-concept, we predominantly used human cell lines throughout this technical note. However, we envision that increased model maturity can be achieved by using more representative cell sources, for instance human breast organoids [70, 71] or blood vessel organoids [72]. Through the incorporation of strategies to enhance tissue maturation and cellular interactions within our platform, this work paves the way for the creation of more recapitulative organ-on-chip models that can bring about advanced disease modeling applications in future studies.

4. Methods

4.1. Bioreactor fabrication

Bioreactor designs were generated in Fusion360 and all CAD and CAM files can be found as editable STEP files and as stl files in the OSF repository [38]. Bioreactor iterations were 3D printed from white PETG (123-3D Filament Wit 1, 75 mm PETG 1 kg (Jupiter serie)) at a layer height of 0.15 mm with ironing enabled for all top surfaces. The final bioreactor design was milled from transparent and autoclavable 5 mm polycarbonate (kunststofplatenshop.nl; polycarbonaat helder 5 mm) using a Sainsmart3040 CNC and end mills of different sizes (0.8 mm, 1 mm, 2 mm, 3 mm) suitable for soft plastics (Stepcraft; End mill set 'low melting plastics' (11706)). As clamps were not in direct contact with cells or printed chips, they were 3D printed from white PETG. To assemble the bioreactors, two components of PDMS were mixed (Dow, SYLGARD™ 182 Elastomer kit) and pipetted into the gasket of the bioreactor bottom. A 0.1 mm glass cover slide was stuck onto the PDMS to the bottom of the bioreactor. A 20 × 2 mm silicone O-ring (Amazon.de; BGS O-Ring Assortment 3–22 mm diameter, PACK of 225 + 8044) was inserted into the round gasket of the bioreactor lid. Bottom and lid of the bioreactor were connected using the clamps. Before use of the bioreactor bottom and lid were autoclaved to ensure sterility.

4.2. Design and fabrication of cell seeding equipment

Inspired by the gel flipper described by Kinstlinger *et al* [20] a rotating station was designed. All parts needed to build the rotator can be found in supplementary table 1 and design files in the OSF repository [38]. 3D printed parts were designed in Fusion360 and printed from PLA (123-3D Filament zwart 1, 75 mm PLA 1, 1 kg (Jupiter serie)) on a Prusa i3 MK3S at a layer height of 0.2 mm. To improve stability, support was added on both sides connected by aluminum extrusions and a leadscrew. In the middle of the leadscrew a 3D printed holder was attached which fits both 15 cm petri dishes and regular sized well plates (suppl. figure 1(A)). Along with that a stamp to mold PDMS inside 15 cm petri dishes to hold up to 4 bioreactors per dish was designed. This setup allowed seeding of chips both already mounted into bioreactors, as well as within well plates, when screenings of many conditions required seeding of many chips at the same time. Well plates, as well as petri dishes, were sealed with parafilm before starting the flipping process, to ensure sterility despite vibrations during the rotation process. In Arduino IDE, the arduino nano

was programmed to turn the dish holder by 90° every 15 min. The script can be found in the OSF repository [38].

4.3. Hydrogel preparation

GelMA (80% degree of functionalization, synthesized as previously described [73]) was weighed under sterile conditions and dissolved in phosphate-buffered saline (PBS) without calcium and magnesium (PBS0) at 6% w/v and mixed with photoinitiator lithium phenyl(2,4,6-trimethylbenzoyl)phosphinate, (LAP, Tokyo Chemical Industry, Japan) at a final concentration of 0.1% w/v. GelMA was kept in the dark at 37 °C until used. 1 ml or 2 ml of GelMA were filled into 10 mm or 20 mm glass vials, respectively. Vials were closed with a silicone plug and GelMA was allowed to thermally gelate in the dark on ice for 10 min.

4.4. Chip fabrication and mounting

The hydrogel-made chip structures were designed with Fusion360 and converted to printable STL files. Design files can be found in the OSF repository [38]. Chips were printed either horizontally (20 mm vials) or vertically (10 mm vials) using a commercial volumetric bioprinter (Tomolite, Readily3D SA) at a light dose of 180–215 mJ cm^{-2} from 6% w/v GelMA. Immediately after printing, uncured GelMA was washed away using warm PBS0 and chip channels were thoroughly flushed with PBS0 and examined for openness of the channels. All chips were post cured in PBS with 0.1% w/v LAP in the UV oven for 2 min. Subsequently, chips were either inserted into bioreactors or mounted into 24-well plates. Chips were fixed in place in 24-well plate wells by spreading a thin layer of 10% w/v GelMA onto the bottom of the well before adding the chip and UV cross-linking it to the chip for 2 min.

4.5. Assessment of print accuracy

To assess printing accuracy, we stained our GelMA with Cy3.5 (Cy3.5-PEG-SH, Biopharma PEG Scientific Inc; FL077003-5 K) prior to printing. Using a custom-built light-sheet microscope we scanned the different chip versions. Chips were segmented using Imaris and the 3D reconstruction exported to wrl-format. In Meshlab software, wrl files were converted to stl format. Reference stl files and reconstructed files were aligned in CloudCompare using ICP fine registration. Absolute deviations were calculated using cloud-to-cloud distance computation and exported to csv. In R we calculated original point coordinates (Reconstructed_Coordinate + (C2M_signed_distanced * Nominal vector)) and subsequently percentage deviations which were back projected onto the reconstructed mesh as a scalar field (suppl. figure 2(A)). Print deviations were further compared to the predicted light accumulations calculated automatically by Apparite software (Readily3D), which estimates the light dose delivered in every voxel of the print, starting from the cumulation of the 2D projections delivered at every angle of rotation of the vial during the tomographic printing process. The light dose values are defined by the tomographic algorithms that govern the printing process and, therefore, are known and can be accurately calculated by the printer's software.

4.6. Coating of the printed channels within the chips

Different coatings were applied to the chips depending on the intended cell types to be cultured in the system. Both 10 mM L-Dopamin (L-DOPA, Sigma Aldrich; 53587-29-4) and Poly-L-Lysine (PLL, Sigma Alrich) were injected into channels and incubated for 30 min at 37 °C before flushing channels with cold PBS0. For multimaterial coatings, a 3 mg ml^{-1} collagen-1 solution (col-1; Corning, rat tail, CLS354236) was mixed with PLL and BME (Basement Membrane Extract, Cultrex RGF BME type 2, R&D systems, 3533-005-02) to final concentrations of 2 mg ml^{-1} col-1, 30% v/v PLL, 1% v/v BME. The mixture was injected into channels and incubated for 10 min at 37 °C. Subsequently, channels were flushed with ice cold 20 X PBS. For fibrin coatings, fibrinogen and thrombin were mixed 1:1 on ice to a final concentration of 2 mg ml^{-1} fibrinogen and 2 U ml^{-1} thrombin. The fibrin solution was injected into channels and incubated at room temperature for 2 min before flushing the channels with ice cold PBS0. All chips were rotated into all directions before flushing the coating out of the chips to ensure that the coating reaches all sides of the channel.

4.7. Cell expansion and culture

MCF10A normal epithelial cells (ATCC CRL-10317™) were cultured according to manufacturers recommendations. Briefly, MCF10A cells were seeded in T75 culture flasks and MCF10A medium (Advanced DMEM + 5% v/v Horse serum + 1% v/v P/S + 20 ng μl^{-1} EGF + 0.5 $\mu g\ ml^{-1}$ Hydrocortisone + 10 μM Forskolin + 10 $\mu g\ ml^{-1}$ Human insulin (Sigma 11061-68-0)) was added and refreshed once a week. Once confluent, cells were split at a 1:6 ratio.

For the vascular co-culture, GFP-HUVECs were cultured in cell culture flasks coated with 0.1% w/v gelatine. Endothelial cell growth medium-2 (EGM-2 MV Microvascular Endothelial Cell Growth Medium-2 BulletKit; Lonza; CC-3202) was refreshed twice a week. Once a week, HUVECs were split at a 1:3 ratio. MSCs were cultured in cell culture flasks coated with 0.1% w/v gelatine. MSC medium (10% FCS, 1% pen/strep, 1% asap in alpha-MEM (Gibco)) was refreshed twice a week. Once a week, MSCs were split at a 1:3 ratio. All cell cultures were kept in a humidified atmosphere of 95% O_2 and 5% CO_2 at 37 °C.

4.8. Chip seeding and culture

Prior to cell seeding, all liquid around and inside the chips was removed and chips were dried at 37 °C until cells were prepared for seeding (∼30 min). MCF10A, HUVECs, MSCs and MBOs were trypsinized into single cells and counted. Cells were resuspended in their respective culture medium at different densities (7.5 M ml^{-1}, 15 M ml^{-1}, 30 M ml^{-1}, 60 M ml^{-1} for MCF10A; 20 M ml^{-1} for HUVECs) and injected into channels. Bioreactors were clamped closed and inserted into PDMS inserts in 15 cm petri dishes, which were wrapped with parafilm. Multiwell plates were wrapped with parafilm. Multiwell plates and petri dishes were inserted into the gel rotator and secured with the belt. Chips were rotated at 37 °C for 6 h, rotating by 90° every 10 min. Subsequently, warm culture medium was added around the chips but not covering the top of the chip to prevent media from flushing freshly seeded cells out of the channel. Chips were seeded a second time two days later. From day three after the second seeding, culture medium was not only refreshed twice a week but also freshly injected into the channels twice a day if no perfusion was applied.

4.9. Immunofluorescent stainings and confocal imaging

Stainings were performed as previously described [56]. Briefly, chips were fixed in cold PFA (4% w/v) for 1.5 h on a rocker at 4 °C. Samples were washed with PBT (PBS + 0.1% w/v Tween20) and kept in PBT until further processed. Before staining, samples were washed in WB2 (1 l PBS + 1 ml of Triton X-100 + 2 ml of 10% (w/v) SDS + 2 g BSA) for 30 min at 4 °C. Epithelial channels were stained for rabbit-anti-cytokeratin-14 (1:1000, Biolegend; 905301), mouse-anti-cytokeratin-8/18 (1:500; Abcam; ab17139), and rat-anti-E-cadherin (1:200; Thermo Fisher; 13-1900) in WB2 overnight. The next day, samples were washed 3× for 1.5 h in WB2. Samples were stained for DAPI (1:1000; Thermo Fisher Scientific Invitrogen™ D1306), Phalloidin-Atto700 (1:200; SigmaAldrich 79286-10 NMOL) and donkey-anti-mouse-AF555 (1:200, Thermo Fisher Scientific; A31570), donkey -anti-rabbit-AF647 (Thermo Fisher Scientific; A31573) and donkey-anti-rat-AF594 (Thermo Fisher Scientific; A21209) over night at 4 °C. Endothelial channels were further stained for CD31-AF488 (1:200; Biolegend; 102513). The next day samples were washed 3 × 1.5 h in WB2, vibratome cut into 350 μm slices and mounted onto thin glass slides. Imaging was executed on a Leica Stellaris confocal microscope using 25× magnification. Chips were evaluated for cell coverage and location of the markers of interest.

4.10. Assessment of cell coverage

Using segmentation in Imaris imaging software 10.1 (Oxford Instruments) we generated a mask of the outline of the channel through manual segmentation and of the cells through intensity-based segmentation. To account for possible inaccuracies in manual segmentation, we expanded the channel mask inwards and outwards. Masked data was imported to python. From the center point (start point) of the channel we computationally approached every point on the outer circumference of the channel (target point) checking for positive values in the cell mask. Once a positive value was found, this target point was considered covered. Every point on that outer circumference was thereby classified into cell-covered and not cell-covered and the percentage of cells covering the channel surface was calculated from the total amount of target points (suppl. figure 2(B)). The script to calculate channel coverage can be found in the OSF repository [38].

4.11. Perfusion startup

To ensure wiggle-free perfused culture, we designed, and 3D printed a perfusion tray, holding the media bottle, bioreactor and tubing in place. The tray holds a 5.5 cm glass bottle and an 8 cm petri dish. Further, clips with different diameter indentations were printed that slide onto triangular extrusions to hold different sizes of tubing in place. Additionally, four pins were printed to secure the tubing on the pumps side. All non-3D-printed components were autoclaved, ahead of perfusion experiments. 3D printed components were cleaned with ethanol and allowed to air dry. The setup was assembled and perfused with PBS to check for leaks. Subsequently, the setup was flushed with Advanced DMEM supplemented with 5% v/v P/S, 5% v/v Glutamax and 5% v/v HEPES (F+++) to prime all tubings and connectors. F+++ was then replaced by the desired culture media. For perfused culture of endothelial channels, MSC and HUVEC medium were mixed at a 1:1 ratio.

Chips were inserted into the bioreactor and care was taken to properly align the lid with help of the guide extrusions. Soft tubing (TackleShop.nl B.V; Cresta Superstretch Silicone Tube 1 m 0.4 mm) was inserted into the channel through the holes in the lid until the resistance of the channel curvature could be felt. Suction and pumping were applied at the same time to facilitate smooth perfusion. Perfusion was started at the lowest possible setting of our pump setup (80 μl h^{-1}) and gradually increased over the coming days, when cells were found to withstand the shear stress. Chips were perfused for up to three weeks. Media was refreshed weekly.

4.12. Evaluation of barrier function using FITC-inulin

Cell-free chips, cellular chips that were cultured under static culture conditions and cellular chips that were cultured under perfused conditions were injected with FITC-Inulin (Merck, F3272-1 G). Using the Leica Thunder imaging system time lapses of the

FITC signal were recorded at 2 min intervals. Imaging data was segmented manually to generate a mask of the channel and the increase of FITC signal outside the boundaries of the channel was quantified over time using a python analysis script [38] (suppl. figure 2(e)).

4.13. Assessment of basal-luminal cellular organization

Using segmentation in Imaris imaging software we generated a mask of the outline of the channel through manual segmentation and of the cells positive for K8/18 and K14 through intensity-based segmentation. To account for possible inaccuracies in manual segmentation we expanded the channel mask inwards and outwards. Masked data was imported to python. From the center point (start point) of the channel we computationally approached every point on the outer circumference of the channel (target point) checking for positive values in the two cell masks. If the first match found in the K8/18 mask, this circumference point was considered *covered by a luminal cell first*. The percentage of circumference points covered by luminal cells was calculated. Further, the percentage of circumference points for which first a signal from the K8/18 mask was obtained followed by a signal from the K14 mask was calculated and named *Correct basal luminal organization* (suppl. figure 1(C)). The script to calculate channel coverage can be found in the OSF repository [38].

4.14. Assessment of cell alignment

Cells covering the channel surface were segmented using intensity-based segmentation in Imaris and the ratio of each cells' bounding box in Z- and Y-direction was calculated. When the bounding box was longer in Z-direction than in Y-direction, it was considered longitudinally aligned (suppl. figure 2(d)). Alignment of cells was quantified using a custom R script which is free to download in our OSF repository [38].

4.15. Statistical analysis

Results were reported as mean ± standard deviation. Statistical analysis was performed in GraphPad Prism 9. Comparisons between experimental conditions was assessed via One-way ANOVA followed by Tukey's multiple comparisons test. For comparison of less than three groups unpaired parametric t test or Welch's t test were performed. Results were considered significant with a p-value < 0.05.

Data availability statement

The data that support the findings of this study are openly available at the following URL/DOI: https://osf.io/gtqf4/?view_only=d22b7cc53c57486198835443d7d6e006.

Acknowledgment

We thank Marc Falandt and Margo Terpstra for providing GelMA and GFP-HUVECs. We thank Mario Barrera Román, Sammy Florczak and the Princess Máxima Imaging Center for support with microscopy.

R.L acknowledges funding from the European Research Council (ERC) under the European Union's Horizon 2020 research and innovation programme (Grant Agreement No. 949806, VOLUME-BIO), and from the Dutch Research Council (NWO VIDI, Grant No. 20387; Gravitation Program 'Materials Driven Regeneration', 024.003.013).

Conflict of interest

R.L. is scientific advisor for Readily3D, which did not participate in or bias the work. The other authors declare no competing interests.

ORCID iDs

Maj-Britt Buchholz https://orcid.org/0000-0003-3058-8485
Paulina Nunez Bernal https://orcid.org/0000-0002-0875-5438
Riccardo Levato https://orcid.org/0000-0002-3795-3804
Anne Rios https://orcid.org/0000-0002-9082-8068

References

[1] Brassard J A and Lutolf M P 2019 Engineering stem cell self-organization to build better organoids *Cell Stem Cell.* **24** 860–76
[2] Nelson C M and Bissell M J 2006 Of extracellular matrix, scaffolds, and signaling: tissue architecture regulates development, homeostasis, and cancer *Annu. Rev. Cell. Dev. Biol.* **22** 287–309
[3] Petzold J and Gentleman E 2021 Intrinsic mechanical cues and their impact on stem cells and embryogenesis *Front. Cell Dev. Biol.* **9** 761871
[4] Norman G A V 2019 Limitations of animal studies for predicting toxicity in clinical trials: is it time to rethink our current approach? *JACC Basic Transl. Sci.* **4** 845–54
[5] Zhao C 2023 Cell culture: *in vitro* model system and a promising path to *in vivo* applications *J. Histotechnol.* **46** 1–4
[6] Bana E and Bagrel D 2011 In vitro breast cancer models as useful tools in therapeutics? *Breast Cancer—Focusing Tumor Microenvironment, Stem Cells and Metastasis* (InTech) ch 2 (https://doi.org/10.5772/21124)
[7] Arslan-Yildiz A, Assal R E, Chen P, Guven S, Inci F and Demirci U 2016 Towards artificial tissue models: past, present, and future of 3D bioprinting *Biofabrication* **8** 014103
[8] Moroni L, Burdick J A, Highley C, Lee S J, Morimoto Y, Takeuchi S and Yoo J J 2018 Biofabrication strategies for 3D in vitro models and regenerative medicine *Nat. Rev. Mater.* **3** 21–37
[9] Levato R, Jungst T, Scheuring R G, Blunk T, Groll J and Malda J 2020 From shape to function: the next step in bioprinting *Adv. Mater.* **32** 1906423
[10] Bayir E, Sahinler M, Celtikoglu M M and Sendemir A 2020 Bioreactors in tissue engineering: mimicking the microenvironment *Woodhead Publishing Series in*

Biomaterials ed N E Vrana, K-M Helena and J Barthes (Woodhead Publishing) ch 27, pp 709–52
[11] Zhao J, Griffin M, Cai J, Li S, Bulter P E M and Kalaskar D M 2016 Bioreactors for tissue engineering: an update *Biochem. Eng. J.* **109** 268–81
[12] Juste-Lanas Y, Hervas-Raluy S, García-Aznar J M and González-Loyola A 2023 Fluid flow to mimic organ function in 3D in vitro models *APL Bioeng.* **7** 031501
[13] Celikkin N *et al* 2021 Tackling current biomedical challenges with frontier biofabrication and organ-on-a-chip technologies *Front. Bioeng. Biotechnol.* **9** 732130
[14] Marshall L E, Goliwas K F, Miller L M, Penman A D, Frost A R and Berry J L 2017 Flow-perfusion bioreactor system for engineered breast cancer surrogates to be used in preclinical testing *J. Tissue Eng. Regen. Med.* **11** 1242–50
[15] Amo C D, Olivares V, Condor M, Blanco A, Santolaria J, Asin J, Borau C and Garcia-Aznar J M 2018 Matrix architecture plays a pivotal role in 3D osteoblast migration: the effect of interstitial fluid flow *J. Mech. Behav. Biomed. Mater.* **83** 52–62
[16] Ng C P, Hinz B and Swartz M A 2005 Interstitial fluid flow induces myofibroblast differentiation and collagen alignment in vitro *J. Cell Sci.* **118** 4731–9
[17] Daems M, Peacock H M and Jones E A V 2020 Fluid flow as a driver of embryonic morphogenesis *Development* **147** dev185579
[18] Kutys M L, Polacheck W J, Welch M K, Gagnon K A, Koorman T, Kim S, Li L, McClatchey A I and Chen C S 2020 Uncovering mutation-specific morphogenic phenotypes and paracrine-mediated vessel dysfunction in a biomimetic vascularized mammary duct platform *Nat. Commun.* **11** 3377
[19] Bernal P N, Delrot P, Loterie D, Li Y, Malda J, Moser C and Levato R 2019 Volumetric bioprinting of complex living-tissue constructs within seconds *Adv. Mater.* **31** e1904209
[20] Kinstlinger I S, Calderon G A, Royse M K, Means A K, Grigoryan B and Miller J S 2021 Perfusion and endothelialization of engineered tissues with patterned vascular networks *Nat. Protocols* **16** 3089–113
[21] Zhang B, Korolj A, Lai B F L and Radisic M 2018 Advances in organ-on-a-chip engineering *Nat. Rev. Mater.* **3** 257–78
[22] Ingber D E 2022 Human organs-on-chips for disease modelling, drug development and personalized medicine *Nat. Rev. Genet.* **23** 467–91
[23] Bissell M J, Rizki A and Mian I S 2003 Tissue architecture: the ultimate regulator of breast epithelial function *Curr. Opin. Cell Biol.* **15** 753–62
[24] Nelson C M, Vanduijn M M, Inman J L, Fletcher D A and Bissell M J 2006 Tissue geometry determines sites of mammary branching morphogenesis in organotypic cultures *Science* **314** 298–300
[25] Battin D A, Marrs R P, Fleiss P M and Mishell D R J 1985 Effect of suckling on serum prolactin, luteinizing hormone, follicle-stimulating hormone, and estradiol during prolonged lactation *Obstet Gynecol.* **65** 785–8
[26] Glasier A, McNeilly A S and Howie P W 1984 The prolactin response to suckling *Clin. End.* **21** 109–16
[27] Organization G W H 2009 Infant and young child feeding: model chapter for textbooks for medical students and allied health professionals (available at: www.ncbi.nlm.nih.gov/books/NBK148970/#:~:text=When%20a%20baby%20suckles%2C%20the,the%20next%20feed%20(20))
[28] Jiang L and Hassanipour F 2021 In vitro flow visualization in a lactating human breast model *Ann. Biomed. Eng.* **49** 3563–73
[29] Leung C M *et al* 2022 A guide to the organ-on-a-chip *Nat. Rev. Method Primers* **2** 33
[30] Low L A, Mummery C, Berridge B R, Austin C P and Tagle D A 2021 Organs-on-chips: into the next decade *Nat. Rev. Drug Discovery* **20** 345–61
[31] Klotz B J, Gawlitta D, Rosenberg A J W P, Malda J and Melchels F P W 2016 Gelatin-methacryloyl hydrogels: towards biofabrication-based tissue repair *Trends Biotechnol.* **34** 394–407
[32] Peela N, Sam F S, Christenson W, Truong D, Watson A W, Mouneimne G, Ros R and Nikkhah M 2016 A three dimensional micropatterned tumor model for breast cancer cell migration studies *Biomaterials* **81** 72–83
[33] Chen Y, Xue D, Huang D, Li X, Duan Y and Chen B 2025 Biofabrication of tunable 3D hydrogel for investigating the matrix stiffness impact on breast cancer chemotherapy resistance *ACS Biomater. Sci. Eng.* **11** 1417–31
[34] Peter M, Singh A, Mohankumar K, Jeenger R, Joge P A, Gatne M M and Tayalia P 2019 Gelatin-based matrices as a tunable platform to study in vitro and in vivo 3D cell invasion *ACS Appl. Bio Mater.* **2** 916–29
[35] Größbacher G *et al* 2023 Volumetric printing across melt electrowritten scaffolds fabricates multi-material living constructs with tunable architecture and mechanics *Adv. Mater.* **35** e2300756
[36] Rusby J E, Brachtel E F, Michaelson J S, Koerner F C and Smith B L 2007 Breast duct anatomy in the human nipple: three-dimensional patterns and clinical implications *Breast Cancer Res. Treat.* **106** 171–9
[37] Dabbagh S R, Rezapour Sarabi M, Birtek M T, Mustafaoglu N, Zhang Y S and Tasoglu S 2023 3D bioprinted organ-on-chips *Aggregate* **4** e197
[38] Buchholz M-B 2024 Breast-on-a-chip repository (available at: https://osf.io/gtqf4/?view_only=d22b7cc53c5748 6198835443d7d6e006)
[39] Hernández-Hatibi S, Guerrero P E, García-Aznar J M and García-Gareta E 2024 Polydopamine interfacial coating for stable tumor-on-a-chip models: application for pancreatic ductal adenocarcinoma *Biomacromolecules* **25** 5169–80
[40] Maoz B M *et al* 2018 A linked organ-on-chip model of the human neurovascular unit reveals the metabolic coupling of endothelial and neuronal cells *Nat. Biotechnol.* **36** 865–74
[41] Salih A R C *et al* 2021 Extracellular matrix optimization for enhanced physiological relevance in hepatic tissue-chips *Polymers* **13** 3016
[42] Joddar B, Tasnim N, Thakur V, Kumar A, McCallum R and Chattopadhyay M 2018 Delivery of mesenchymal stem cells from gelatin–alginate hydrogels to stomach lumen for treatment of gastroparesis *Bioengineering* **5** 12
[43] Matveeva V G, Velikanova E A, Antonova L V and Barbarash L S 2023 Fibrin coating contributes to the retention of the endothelial layer in pulsating flow *J. Evol. Biochem. Physiol.* **59** 1320–30
[44] Maller O, Martinson H and Schedin P 2010 Extracellular matrix composition reveals complex and dynamic stromal-epithelial interactions in the mammary gland *J. Mammary Gland Biol. Neoplasia* **15** 301–18
[45] Alberts B, Johnson A, Lewis J, Raff M, Roberts K and Walter P (eds) 2002 Histology: the lives and deaths of cells in tissues *Molecular Biology of the Cell.* 4th edn (New York: Garland Science)
[46] Hall D C, Palmer P, Ji H-F, Ehrlich G D and Król J E 2021 Bacterial biofilm growth on 3D-printed materials *Front. Microbiol.* **12** 646303
[47] Kutluk H, Bastounis E E and Constantinou I 2023 Integration of extracellular matrices into organ-on-chip systems *Adv. Healthcare Mater.* **12** 2203256
[48] Katoh K 2023 Effects of mechanical stress on endothelial cells in situ and in vitro *Int. J. Mol. Sci.* **24** 16518
[49] Blum K M *et al* 2022 Tissue engineered vascular grafts transform into autologous neovessels capable of native function and growth *Commun. Med.* **2** 3
[50] Tarbell J M 2010 Shear stress and the endothelial transport barrier *Cardiovasc. Res.* **87** 320–30
[51] Maggiorani D *et al* 2015 Shear stress-induced alteration of epithelial organization in human renal tubular cells *PLoS One* **10** e0131416

[52] Delon L C, Guo Z, Oszmiana A, Chien C-C, Gibson R, Prestidge C and Thierry B 2019 A systematic investigation of the effect of the fluid shear stress on Caco-2 cells towards the optimization of epithelial organ-on-chip models *Biomaterials* **225** 119521
[53] Ferrell N, Cheng J, Miao S, Roy S and Fissell W H 2018 Orbital shear stress regulates differentiation and barrier function of primary renal tubular epithelial cells *ASAIO J.* **64** 766–72
[54] Sidhaye V K, Schweitzer K S, Caterina M J, Shimoda L and King L S 2008 Shear stress regulates aquaporin-5 and airway epithelial barrier function *Proc. Natl Acad. Sci.* **105** 3345–50
[55] Rein J L, Heja S, Flores D, Carrisoza-Gaytán R, Lin N Y C, Homan K A, Lewis J A and Satlin L M 2020 Effect of luminal flow on doming of mpkCCD cells in a 3D perfusable kidney cortical collecting duct model *Am. J. Physiol. Cell Physiol.* **319** C136–C47
[56] van Ineveld R L *et al* 2022 Multispectral confocal 3D imaging of intact healthy and tumor tissue using mLSR-3D *Nat. Protocols* **17** 3028–55
[57] Macias H and Hinck L 2012 Mammary gland development *Wiley Interdiscip. Rev. Dev. Biol.* **1** 533–57
[58] Liu H, Chansoria P, Delrot P, Angelidakis E, Rizzo R, Rütsche D, Applegate L A, Loterie D and Zenobi-Wong M 2022 Filamented light (FLight) biofabrication of highly aligned tissue-engineered constructs *Adv. Mater.* **34** 2204301
[59] Rackson C, Toombs J T, De Beer M P, Cook C C, Shusteff M, Taylor H K and McLeod R R 2022 Latent image volumetric additive manufacturing *Opt. Lett.* **47** 1279–82
[60] Rizzo R, Rütsche D, Liu H, Chansoria P, Wang A, Hasenauer A and Zenobi-Wong M 2023 Multiscale hybrid fabrication: volumetric printing meets two-photon ablation *Adv. Mater. Technol.* **8** 2201871
[61] Suarez A M A, van der Ham I, Brinker M G L, van Rijn P and Harmsen M C 2020 Topography-driven alterations in endothelial cell phenotype and contact guidance *Heliyon* **6** e04329
[62] Liu H, Kitano S, Irie S, Levato R and Matsusaki M 2020 Collagen microfibers induce blood capillary orientation and open vascular lumen *Adv. Biosyst.* **4** e2000038
[63] Sinha R, Le Gac S, Verdonschot N, van den Berg A, Koopman B and Rouwkema J 2016 Endothelial cell alignment as a result of anisotropic strain and flow induced shear stress combinations *Sci. Rep.* **6** 29510
[64] Bernal P N *et al* 2022 Volumetric bioprinting of organoids and optically tuned hydrogels to build liver-like metabolic biofactories *Adv. Mater.* **34** 2110054
[65] Xu H-Q, Liu J-C, Zhang Z-Y and Xu C-X 2022 A review on cell damage, viability, and functionality during 3D bioprinting *Mil. Med. Res.* **9** 70
[66] Ribezzi D *et al* 2023 Shaping synthetic multicellular and complex multimaterial tissues via embedded extrusion-volumetric printing of microgels *Adv. Mater.* **35** 2301673
[67] Lian L *et al* 2024 Rapid volumetric bioprinting of decellularized extracellular matrix bioinks *Adv. Mater.* **36** 2304846
[68] Falandt M *et al* 2025 Hybrid supramolecular-covalent bioresin promotes cell migration and self-assembly in light-based volumetric bioprinted constructs *bioRxiv Preprint* (https://doi.org/10.1101/2025.01.06.631505) (Accessed 3 February 2025)
[69] Tornberg K, Välimäki H, Valaskivi S, Mäki A-J, Jokinen M, Kreutzer J and Kallio P 2022 Compartmentalized organ-on-a-chip structure for spatiotemporal control of oxygen microenvironments *Biomed. Microdevices* **24**
[70] Qu Y, Han B, Yu Y, Yao W, Bose S, Karlan B Y, Giuliano A E and Cui X 2015 Evaluation of MCF10A as a reliable model for normal human mammary epithelial cells *PLoS One* **10** e0131285
[71] Rosenbluth J M *et al* 2020 Organoid cultures from normal and cancer-prone human breast tissues preserve complex epithelial lineages *Nat. Commun.* **11** 1711
[72] Wimmer R A *et al* 2019 Human blood vessel organoids as a model of diabetic vasculopathy *Nature* **565** 505–10
[73] Levato R, Webb W R, Otto I A, Mensinga A, Zhang Y, van Rijen M, van Weeren R, Khan I M and Malda J 2017 The bio in the ink: cartilage regeneration with bioprintable hydrogels and articular cartilage-derived progenitor cells *Acta Biomater.* **61** 41–53